International Journal of Fatigue 87 (2016) 257–265

Contents lists available at ScienceDirect

International Journal of Fatigue

journal homepage: www.elsevier.com/locate/ijfatigue

Fatigue damage of closed-cell aluminum alloy foam: Modeling and mechanisms

Modi Zhao, Xueling Fan, T.J. Wang *

State Key Laboratory for Strength and Vibration of Mechanical Structures, Department of Engineering Mechanics, School of Aerospace Engineering, Xi'an Jiaotong University, Xi'an 710049, China

ARTICLE INFO

Article history:
Received 3 October 2015
Received in revised form 3 February 2016
Accepted 7 February 2016
Available online 11 February 2016

Keywords:
Metal foam
Closed-cell
Fatigue
Statistical
Mechanism

ABSTRACT

The objective of this work is to experimentally investigate the damage evolution and damage mechanism in closed-cell aluminum alloy foam under tension–tension fatigue loading. Constant amplitude fatigue tests are performed for the aluminum alloy foam, and experimental results indicate the large scatter of the fatigue damage in the aluminum alloy foam. To describe the fatigue damage with large scatter, a statistical fatigue damage model is developed on the basis of continuum damage mechanics. It is seen that the statistical damage model can describe the fatigue damage of the foam. Scanning electron microscopy (SEM) observation on the fracture surface of the tested specimen is carried out to understand the damage mechanisms of the foam. Four major categories of fatigue damage mechanism are concluded, i.e. damage initiates from the material surface, damage initiates on the cell wall, damage initiates at the intersection of several cell walls and damage initiates from the edge of cell. The high-resolution SEM images reveal that the fatigue mechanisms of the foam are mainly governed by the cell structure.

1. Introduction

In the last decades, metal foam has been widely used in a number of engineering structures, such as automobile, aircraft, and spacecraft, and attentions have been devoted to the plasticity, dynamic response and energy absorption of metal foam [1–4]. However, there are relatively few investigations on foam fatigue. Previous studies show the large scatter characteristic of the foam fatigue [5–15]. Based on the tension–compression fatigue experimental results of two kinds of metal foams, Zettl et al. [6] demonstrated a pronounced scatter in the lifetimes of the foams. McCullough et al. [7] performed tension–tension fatigue and compression-compression fatigue of closed-cell aluminum alloy foams. Through compression-compression fatigue experiments, Kolluri et al. [8] investigated the mechanical behavior of foam under lateral constant. In both cases, it was found that the fatigue of foams is highly sensitive to the applied stress. Zenkert and Burman [9] compared the tensile, compressive and shear fatigue testing of closed-cell foam with different densities, and found that different load types exhibit different failure mechanisms. Kanny et al. [10] conducted flexural fatigue tests on cross-linked PVC foams over a wide range of density. It was shown that the flexural fatigue strength of the foams increased as the density increased. Significant scatter of the fatigue properties was also reported for open cell aluminum foams [13]. The larger scatter characteristic of fatigue property makes it difficult to study the fatigue behavior of foam materials.

Previously, various methods were adopted to study the fatigue behavior of materials. Among them, the continuum damage mechanics (CDM) was most commonly used in the framework of continuum mechanics and continuum thermodynamics [16–20]. CDM gives a better understanding of the state of materials by the definition of one or several continuum damage variables representing the material degradation. In all these studies major emphasis was put on the development and application of deterministic damage models. However, in their current form, these deterministic damage models are valid only for predicting fatigue properties of materials without large scatter [18,20].

Existing literature shows that the structure is a key factor leading to the scatter of mechanical properties of foams [21–27]. Ramamurty and Paul [21] experimentally studied the variability in the elastic modulus, plastic strength, and energy absorption of a closed-cell Al foam. By considering the micro-mechanism of deformation in the closed-cell foam they related the variability of mechanical properties to the variance in the cell-size. Zhu and Windle [22] found that compared to regular foam highly irregular foam has a lower effective stress at high compressive strains. The

* Corresponding author. Tel.: +86 29 82663318; fax: +86 29 82669044.
E-mail address: wangtj@mail.xjtu.edu.cn (T.J. Wang).

http://dx.doi.org/10.1016/j.ijfatigue.2016.02.009
0142-1123/

experiments performed by Kolluri et al. [8] and Simon and Gibson [23] illustrated that the defect distribution and orientation with respect to the loading directions have major impact on the scatter of mechanical properties of metal foams. Brothers and Dunand [24] found that the pore size has significant effect on the flow stress. The influences of inhomogeneous micro-structure on stress distribution and fracture of cell walls had been studied by Andrews et al. [25]. Our recent work on the fatigue of closed-cell aluminum alloy foam showed that the fatigue life decreases as the number and the size of large cell increase [26]. Scanning electron microscopy (SEM) studies were performed to examine the dependence of lifetime on the inhomogeneous structure of the foams [5,6]. While there have been some progress in the study of fatigue damage of metal foams, understanding of the dependence of fatigue property variability on the structure characteristics of foam is still very limited [27].

In this paper, the damage evolution and damage mechanisms in closed-cell aluminum foam material are investigated. The paper is organized as follows. Experimental details are presented in Section 2. The statistical fatigue damage model is derived in Section 3, and analysis of the fatigue damage mechanisms is presented in Section 4. Finally, concluding remarks are summarized in Section 5.

2. Experimental

2.1. Material and specimens

The closed-cell aluminum alloy foam examined in this study was provided by the Material Institute of Luoyang, China. The foam has an average relative density ρ of 28.7%. Dog-bone shape specimens were used for both static and fatigue tests. The dimensions of specimen are shown in Fig. 1, in which the black frame indicates the gauge section of 50 mm × 20 mm × 20 mm. Static properties of the foam were tested at room temperature by using the universal MTS 880 machine. Three specimens were tested at a crosshead speed of 2 mm/min. An extensometer was used to monitor the strain within the gauge section. The load and strain were recorded by using a computer data-acquisition system. The average value of tensile strength is 9.27 MPa. Details on the material and its static properties can be found in a previous study [26].

2.2. Fatigue tests

Due to the fact that no fatigue test standard is available for foam material, we referred to the ASTM standard (ASTM E466-07) herein for the fatigue tests of foam material. The universal MTS 880 machine was employed to carry out the tension–tension fatigue tests. Constant amplitude fatigue loads with a sinusoidal waveform and a stress ratio $R = 0.1$ ($R = \sigma_{min}/\sigma_{max}$ with σ_{min} and σ_{max} being the minimum and maximum stresses in one load cycle) were applied. The loading frequency was 20 Hz. Four stress levels with maximum tensile stresses of 7 MPa, 6.5 MPa, 6 MPa and 5.5 MPa, respectively, were considered and a total of 13 dog-bone shape specimens shown in Fig. 1 were tested. An extensometer was used to monitor the strain within the gauge section. The load and strain were continuously recorded by using the computer data-acquisition system. All the fatigue tests were conducted at room temperature.

It should be noted that due to the relatively low compression performance of foam the specimens could be easily destroyed by the testing machine. Thus, the specimens could not be directly fixed to the testing machine. In this study, loading fixtures were specially designed, as shown in Fig. 2, in which the specimen was indicated by the cellular pattern and the fixtures were daubed on gray color. The specimen was firstly bonded to the fixtures and then the fixtures were connected to MTS hydraulic grips.

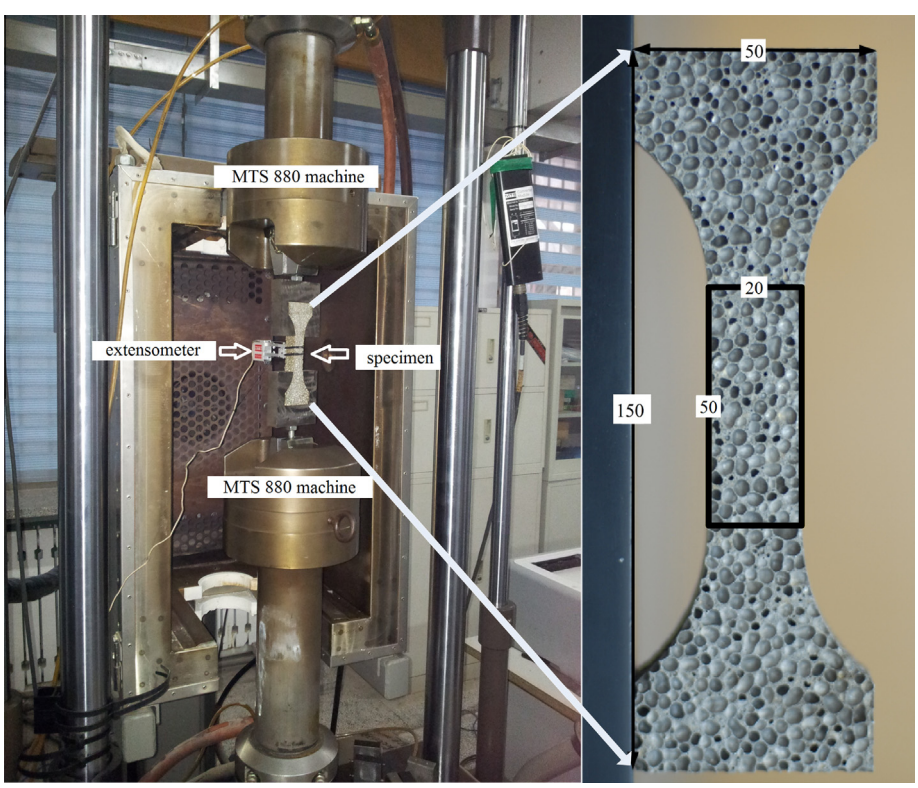

Fig. 1. Dimensions of the closed-cell aluminum foam specimen (mm).

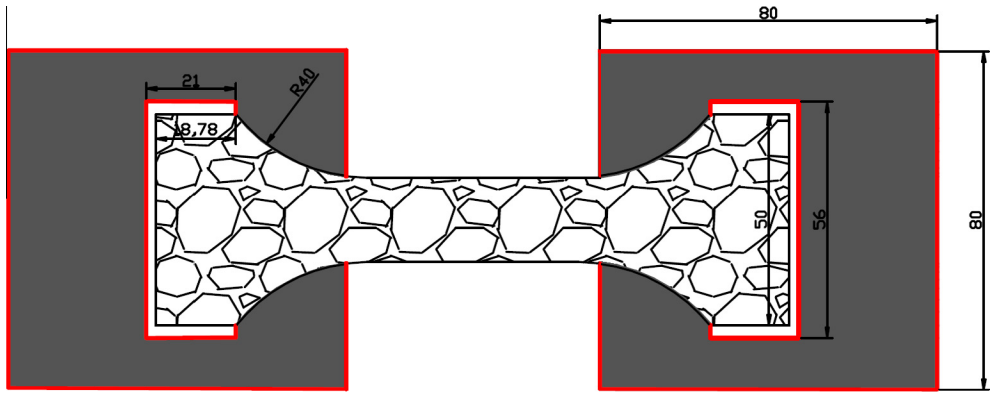

Fig. 2. Specimen and the specially designed fixtures (mm).

2.3. Microscopic observation of fracture surface

Microscopic observation of the fracture surface was performed by using SEM FEI Quanta 400 to understand the damage mechanisms of the foam. Considering the size of the specimen and the chamber space of Quanta 400 machine, the fractured specimens were firstly divided into small sections. Then, selected sections were put into the chamber of SEM machine and the fracture surfaces were observed. Based on the microstructure observations, the mechanisms of fatigue damage of the foam were examined.

2.4. Experimental results

According to the slopes of cyclic stress–strain curves at different cycles, as schematically shown in Fig. 3, we can calculate the apparent elastic modulus within each loading cycle. The variation of the elastic modulus with loading cycle is shown in Fig. 4 for specimens tested under four different loading levels of 5.5 MPa, 6.0 MPa, 6.5 MPa and 7.0 MPa.

In Fig. 4, the apparent elastic modulus E is normalized by its initial value E_0, while the number of loading cycle N is normalized by the fatigue life N_F. It is seen clear that the elastic modulus decreases gradually with the increase of loading cycle until failure occurs, where an abrupt drop of apparent elastic modulus is observed.

Significant scatter of the stiffness degradation is observed, as shown in Fig. 4. The scatter of stiffness degradation is comparable for each stress level. In other words, the scatter of stiffness degradation is independent of the stress. At the same time, we fixed the

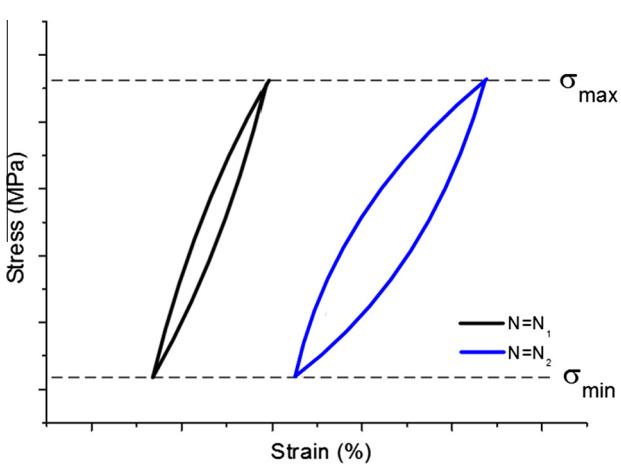

Fig. 3. Schematic diagram for the hysteresis loops at two different cycles N_1 and N_2 ($N_2 > N_1$).

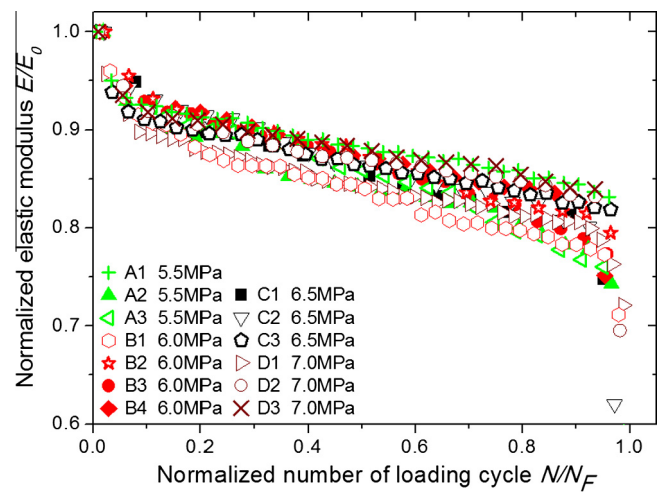

Fig. 4. Stiffness degradation under different loading levels of 5.5 MPa, 6.0 MPa, 6.5 MPa and 7.0 MPa. Different colors and shapes represent different specimens. (For interpretation of the references to color in this figure legend, the reader is referred to the web version of this article.)

dimensions of the specimens and all other test conditions in this study. As a consequence, the specimen-to-specimen variability induces the scatter of stiffness.

Generally, the damage of material is induced by the existence and development of micro-defects. So a reduction of the effective bearing area of material is induced by material damage. This reduction inevitably leads to the change of material performances, such as elastic modulus, etc. Therefore, we adopted the definition the damage variable D using the variation of elastic modulus, e.g. Lemaitre and Dufailly [28], which can be experimentally measured:

$$D = 1 - \frac{E}{E_0} \tag{1}$$

Based on the experimental data shown in Fig. 4 and the definition of damage variable D [28], we obtain the damage evolution of the foam, as shown in Fig. 5. One can see a significant scatter of the fatigue damage. Similar to previously discussion of the stiffness degradation, the specimen-to-specimen difference is the primary cause of the scatter in fatigue damage evolution.

3. Statistical fatigue damage model

If a damage variable D is defined, the evolution of fatigue damage can be examined. In the framework of CDM, a number of models were proposed to describe the damage evolution of

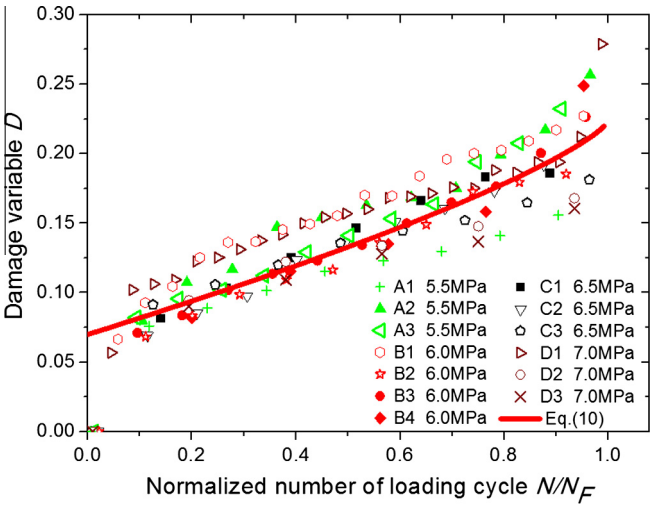

Fig. 5. Damage evolution of specimens tested under different fatigue loading levels. The red line is obtained based on Eq. (10). (For interpretation of the references to color in this figure legend, the reader is referred to the web version of this article.)

materials [16–20]. For example, Lemaitre and Plumtree [16] proposed a continuum damage model for the fatigue of materials. Wang and Lou [17] proposed a nonlinear damage model for low cycle fatigue of materials.

Fatigue damage is generally related to the material deformation. In this work, we focused on the high cycle fatigue of foam material. There exist very local plastic deformation in the material and the overall behavior of the material is still in elastic state. The local plastic deformation may induce local damage, so we adopted the idea of Lemaitre et al. [29–31] to use the microscopic plastic strain range $\Delta\pi$ to derive the damage evolution equation. Herein, we choose the following dissipation potential,

$$\Phi = \frac{S}{r+1}\left(\frac{-Y}{S}\right)^{r+1}\frac{\Delta\dot{\pi}}{(1-N/N_F)^{1-\alpha}} \tag{2}$$

where S, r and α are material constants, N is the number of fatigue cycles, N_F is the number of critical cycle to fatigue failure, respectively. The damage strain energy release rate Y can be calculated as [17–19,29–31],

$$-Y = \frac{\Delta\overline{\sigma}_{eq}^2}{2E} f\left(\frac{\sigma_m}{\sigma_{eq}}\right) \tag{3}$$

where equivalent effective stress range $\Delta\overline{\sigma}_{eq} = \frac{\Delta\sigma_{eq}}{1-D}$ with $\Delta\sigma_{eq}$ being equivalent stress range; the stress triaxiality function $f\left(\frac{\sigma_m}{\sigma_{eq}}\right) = \frac{2}{3}(1+\nu) + 3(1-2\nu)\left(\frac{\sigma_m}{\sigma_{eq}}\right)^2$ with ν, σ_m and σ_{eq} being Poisson's ratio, hydrostatic stress and von Mises equivalent stress, respectively. The microscopic plastic strain range can be calculated as [18]:

$$\Delta\pi = \left(\frac{\Delta\overline{\sigma}_{eq}}{K}\right)^m \tag{4}$$

where K and m are material constants.

According the theory of CDM, the equation of damage evolution can be derived as,

$$\dot{D} = -\frac{\partial\Phi}{\partial Y} = \left(-\frac{Y}{S}\right)^r \frac{\Delta\dot{\pi}}{(1-N/N_F)^{1-\alpha}} \tag{5}$$

From Eqs. (3)–(5), we have

$$\dot{D} = \left(-\frac{Y}{S}\right)^r \frac{m}{K^m}\frac{(\Delta\overline{\sigma}_{eq})^{m-1}\Delta\dot{\overline{\sigma}}_{eq}}{(1-N/N_F)^{1-\alpha}} = B\left[f\left(\frac{\sigma_m}{\sigma_{eq}}\right)\right]^r \frac{(\Delta\overline{\sigma}_{eq})^{\beta}\Delta\dot{\overline{\sigma}}_{eq}}{(1-N/N_F)^{1-\alpha}} \tag{6}$$

where $\beta = 2r + m - 1$ and $B = m/(2ES)^r K^m$ are material constants. In the case of proportional loading, the stress triaxiality σ_m/σ_{eq} can be considered as a constant, and the damage per cycle can be obtained by integrating Eq. (6),

$$\begin{aligned}\frac{\delta D}{\delta N} &= 2\int B\left[f\left(\frac{\sigma_m}{\sigma_{eq}}\right)\right]^r \frac{(\Delta\overline{\sigma}_{eq})^{\beta}}{(1-N/N_F)^{1-\alpha}} d(\Delta\overline{\sigma}_{eq}) \\ &= \frac{2B}{\beta+1}\left[f\left(\frac{\sigma_m}{\sigma_{eq}}\right)\right]^r \frac{(\Delta\overline{\sigma}_{eq})^{\beta+1}}{(1-N/N_F)^{1-\alpha}}\end{aligned} \tag{7}$$

Integrating Eq. (7) with initial conditions $D|_{N=0} = D_0$ and $D|_{N=N_F} = D_c$, we have

$$D - D_0 = \frac{2B(\Delta\overline{\sigma}_{eq})^{\beta+1}}{\beta+1}\left[f\left(\frac{\sigma_m}{\sigma_{eq}}\right)\right]^r \frac{N_F}{\alpha}\left[1-\left(1-\frac{N}{N_F}\right)^{\alpha}\right] \tag{8}$$

and

$$D_c - D_0 = \frac{2B(\Delta\overline{\sigma}_{eq})^{\beta+1}}{\beta+1}\left[f\left(\frac{\sigma_m}{\sigma_{eq}}\right)\right]^r \frac{N_F}{\alpha} \tag{9}$$

From Eqs. (8) and (9), we have

$$D = D_c - D_d\left(1-\frac{N}{N_F}\right)^{\alpha} \tag{10}$$

where $D_d = D_c - D_0$.

It is seen from Fig. 4 that an early drop of apparent elastic modulus appears. The early drop of the apparent elastic modulus is due to the microstructures, such as dislocation. This makes the material damage is hard to be determined at the early stage of fatigue. In addition, the emphasis of this work is to examine the stabilization stage of the fatigue damage instead of the early stage of stiffness degradation. Therefore, a non-zero limit D_0 is chosen herein for $N = 0$ cycles.

It is seen from Eq. (10) that $D = D_0$ when $N = 0$ and reaches its critical value D_c when $N = N_F$, and the independent variable N/N_F varies from 0 to 1. This equation is formally closed and physically reasonable. When the number of fatigue loading cycle N is normalized by the fatigue life N_F, the N/N_F has the same variation range from 0 to 1 for each specimen.

From the experimental data shown in Fig. 5, we obtain the parameters D_c, D_d and α in Eq. (10), as listed in Table 1. It is found from Table 1 that α is approximately a constant for all the 13 specimens. In contrast, the damage parameters D_c and D_d vary around their average values. The variations of D_c and D_d are shown in Fig. 6 for different stress levels, where D_c and D_d are normalized by their average values D_{cav} and D_{dav}. It is seen from Fig. 6 that the variations of damage parameters D_c and D_d are comparable

Table 1
Material parameters in Eq. (10) for different tested specimens.

Specimen no.	D_c	D_d	α
A1	0.23768	0.18106	0.762
A2	0.19470	0.12369	0.767
A3	0.25872	0.17058	0.758
B1	0.22780	0.16522	0.773
B2	0.20751	0.14595	0.754
B3	0.21129	0.13654	0.769
B4	0.17692	0.10095	0.763
C1	0.17456	0.10469	0.756
C2	0.24838	0.19103	0.752
C3	0.26443	0.20840	0.758
D1	0.22748	0.12897	0.766
D2	0.26033	0.18804	0.763
D3	0.21556	0.15186	0.767
Average	0.22349	0.15361	0.762

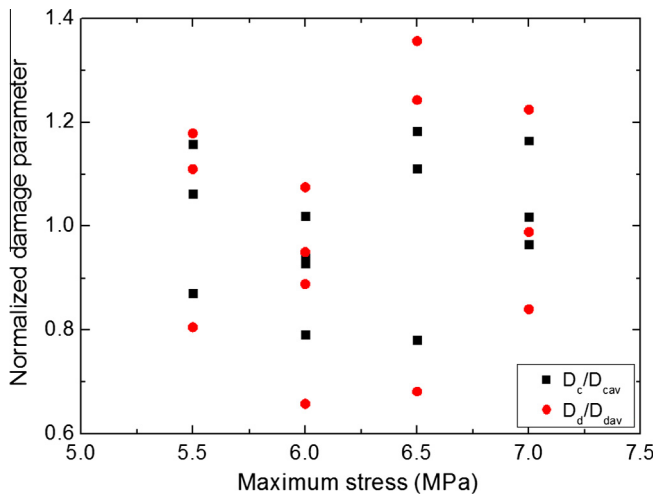

Fig. 6. Variations of damage parameters D_c and D_d.

for different stress levels. The scatters of damage parameters D_c and D_d are independent of the applied stress.

Based on the average values of D_c, D_d and α, we can obtain the average damage evolution curve for the foam, as shown in Fig. 5. Obviously, this curve cannot describe the scatter characteristic of fatigue damage of the foam. So, statistic fatigue damage model is needed. Herein, the normal distribution is adopted to characterize the statistical characteristic of D_c and D_d. The probability density function (PDF) of damage variable D is given by

$$f(D) = \frac{1}{s\sqrt{2\pi}} \exp\left(-\frac{1}{2}\left(\frac{D-\mu}{s}\right)^2\right) \tag{11}$$

where the mathematical expectation is

$$\mu = \frac{1}{n}\sum_{i=1}^{n} D_i \tag{12}$$

and the standard deviation is

$$s = \sqrt{\frac{1}{n-1}\sum_{i=1}^{n}(D_i-\mu)^2} \tag{13}$$

The cumulative distribution function (CDF) of damage variable D is obtained by

$$P(X \leqslant D) = \int_{-\infty}^{D} f(x)dx \tag{14}$$

Table 2
The mathematical expectations and standard deviations of D_c and D_d.

Parameter	Mathematical expectation (μ)	Standard deviation (s)
D_c	0.224	0.035
D_d	0.154	0.039

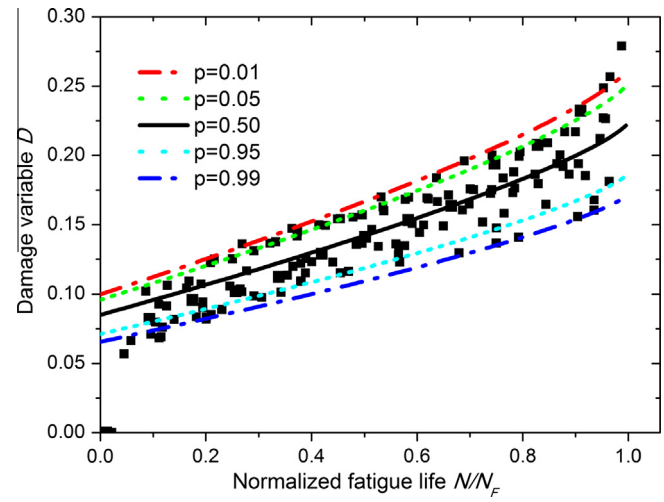

Fig. 7. Statistic damage evolution curves predicted by Eq. (20). The curves with different p values represent the probabilities of different events: the practical fatigue damage is larger than the fatigue damage predicted by these curves.

Substitution of Eqs. (11) into (14) yields

$$P(X \leqslant D) = \frac{1}{2}\left[1 + erf\left(\frac{1}{\sqrt{2}}\frac{D-\mu}{s}\right)\right] \tag{15}$$

where $erf(x)$ is the Gauss error function.

From Eq. (15) we can obtain the following CDFs of D_c and D_d

$$P(X \leqslant D_c) = \frac{1}{2}\left[1 + erf\left(\frac{1}{\sqrt{2}}\frac{D_c-\mu}{s}\right)\right] \tag{16}$$

$$P(X \leqslant D_d) = \frac{1}{2}\left[1 + erf\left(\frac{1}{\sqrt{2}}\frac{D_d-\mu}{s}\right)\right] \tag{17}$$

From Eqs. (12) and (13), we obtain the mathematical expectations μ and the standard deviations s of D_c and D_d, as listed in Table 2. Then, the variations of D_c and D_d with probability p can be presented as,

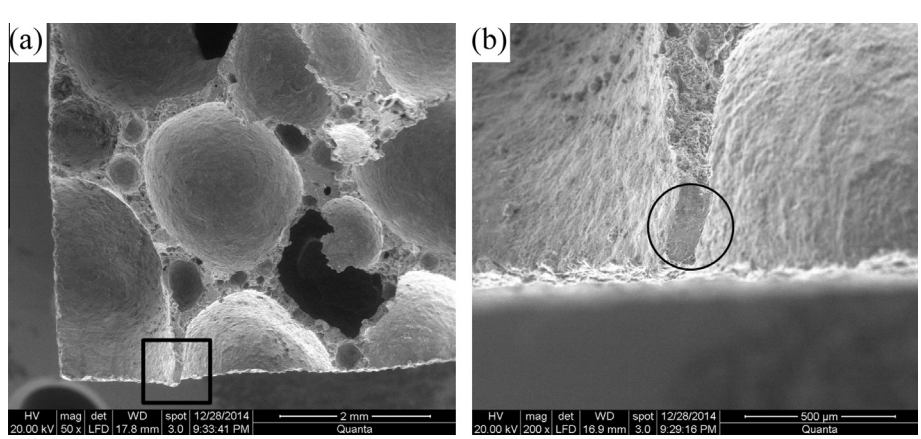

Fig. 8. (a) Typical macroscopic image of the fracture surface. (b) A more detailed view of the damage initiation zone, which is marked with a black square in (a).

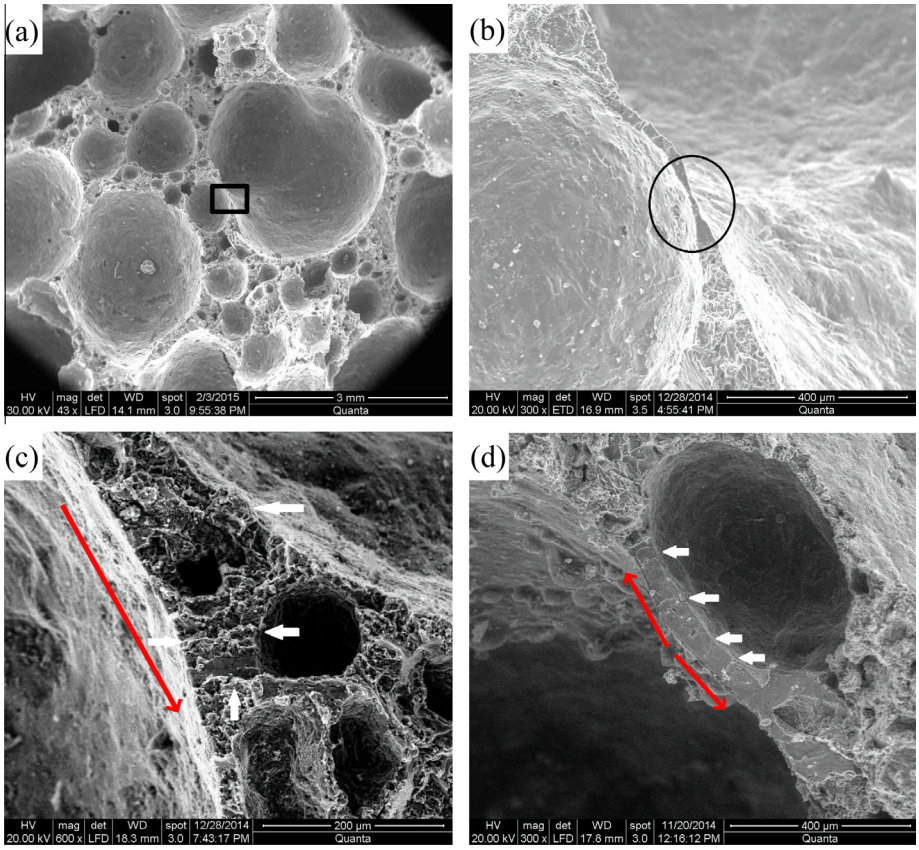

Fig. 9. Damage initiates on the thinnest position of cell wall (marked with black circle). (a) A general view. (b) A more detailed view of the area marked with a black square in (a). (c) and (d) Fatigue striations on the cell walls, in which red and white arrows indicate the damage propagation directions and the fatigue striations, respectively. (For interpretation of the references to colour in this figure legend, the reader is referred to the web version of this article.)

$$(D_c)_p = 0.224 + 0.049erf^{-1}(2p-1) \tag{18}$$

$$(D_d)_p = 0.154 + 0.055erf^{-1}(2p-1) \tag{19}$$

where the $erf^{-1}(x)$ is the inverse function of Gauss error function.

Substituting Eqs. (18) and (19) into (10), we obtain the following statistical fatigue damage model for the foam,

$$D = 0.224 + 0.049erf^{-1}(2p-1) - \left[0.154 + 0.055erf^{-1}(2p-1)\right]\left(1 - \frac{N}{N_F}\right)^{0.762} \tag{20}$$

Based on Eq. (20), the damage evolution as a function of N/N_F are plotted in Fig. 7 for five different probabilities p of 1%, 5%, 50%, 95% and 99%. Here, the value of p represents the probability that the practical fatigue damage is larger than the predicted value. It is seen that the fatigue damage of the foam can be accurately described by the statistical damage model, in which the statistical characteristic of fatigue damage of foam is reflected by the probabilities p.

4. Fatigue damage mechanisms

In the previous study [26], the fracture surfaces were examined using a low magnification optical camera to analyze the scatter of fatigue life. In this work, we focus on the micro-mechanisms of fatigue damage initiation in the foam. To identify the exact initiation sites and propagation directions of crack, a high magnification SEM is used to conduct the micro-observations in the current paper.

Fig. 8(a) shows a typical macroscopic image of the fracture surface. Fig. 8(b) shows a higher magnification of Fig. 8(a) and thus a more detailed view of the damage initiation zone (marked with a black square in Fig. 8(a)) can be seen. A much smoother zone than its surrounded regions can be distinguished, as marked with a black circle in Fig. 8(b). Based on the difference between the smooth zone and its neighboring regions, we can infer that it is one of the damage initiation positions. It is the damage initiates from material surface, which is the first category of fatigue damage mechanism of the foam. It should be pointed that the cells exposed to the surface are not strictly closed-cells, which can cause the presence of significant stress concentration. As a result, damage can more easily initiate from these cells than from those fully closed-cells. This observation is similar to that of solid materials.

The second category of fatigue damage mechanism is damage initiation from the interior cell walls, as shown in Fig. 9. A general view of the fracture surface and a more detailed view of the initiation region are presented in Fig. 9(a) and (b), respectively. Analysis of the SEM images reveals that the center of the cell wall (in black circle in Fig. 9(b)) is relatively smoother than other regions, which implies the position of damage initiation. The stress concentration due to irregular cell structure of the foam induced the damage initiation on the cell wall. Once the damage initiation criterion is satisfied, damage initiates from these sites of stress concentration. Mostly, the center position of cell wall is the thinnest position and the stress concentration on thinner cell walls is significantly larger than those on thicker cell walls. Thus, damage preferentially initiates from the thinnest position of cell walls. Similar phenomena were also observed by Zettl et al. [6]. They concluded that fatigue damage is governed by the formations of

damage, which preferentially initiates in the interior sections of cell walls at initial defects.

Typical fatigue striations are observed on the fracture surface and indicated by the white arrows in Fig. 9(c) and (d). The damage growth path on the cell wall is also shown, in which the damage growth directions are marked with red arrows. It is seen that damage propagates along the cell walls. This is a natural choice since the presence of cell serves as an obstacle to crack propagating and provides additional fracture resistance. In this case, a propagating fatigue damage may terminate while reaching the cell wall and kinks off its original path as loading cycle increases. As a result, damage mainly propagates along the cell wall instead of direct to

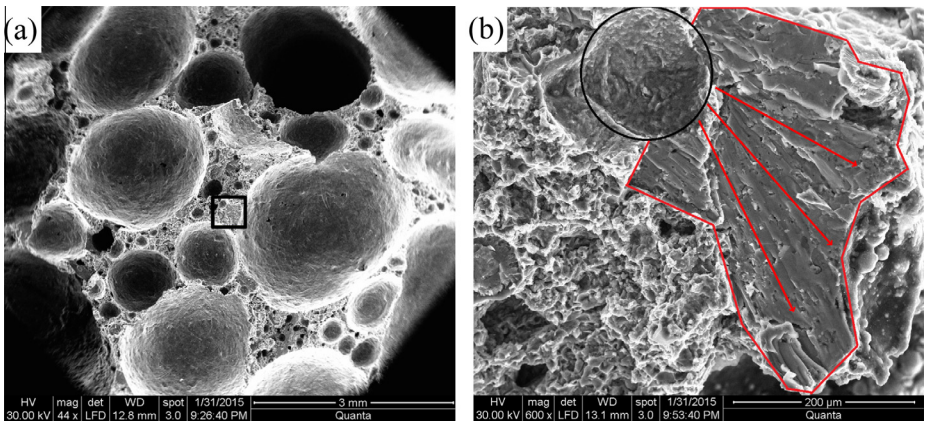

Fig. 10. Damage initiates from the intersection of cell walls: (a) a general view; (b) a detailed view of the damage initiation position and propagation path. The damage propagation regions (marked with red frames) as well as the typical river and radial patterns are presented. Characteristics of typical dimples can be discerned in the final fracture regions. (For interpretation of the references to color in this figure legend, the reader is referred to the web version of this article.)

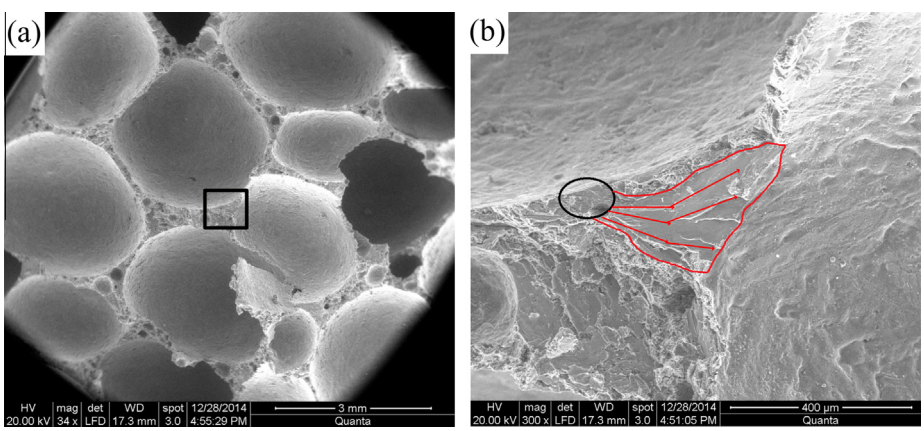

Fig. 11. Damage initiates from one cell and propagates to another one: (a) a general view; (b) a detailed view of the damage initiation position and propagation path. The damage initiate position and the damage propagation regions are marked with a black circle and red frames, respectively. (For interpretation of the references to color in this figure legend, the reader is referred to the web version of this article.)

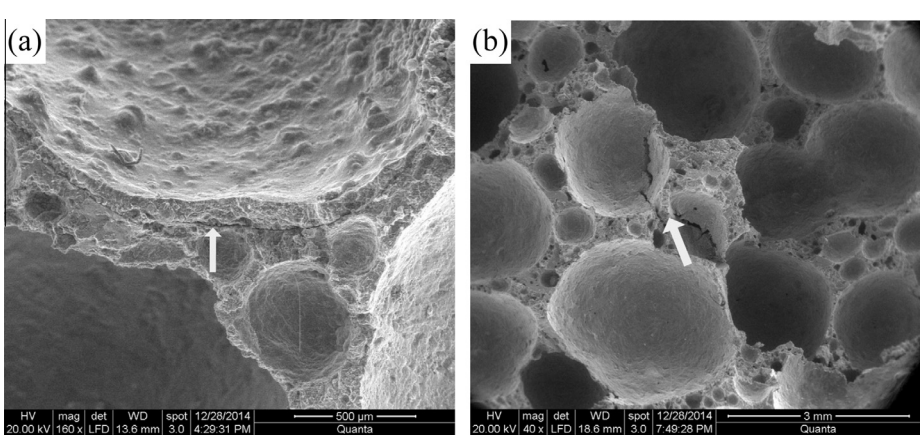

Fig. 12. Secondary cracks observed on the fracture surface of the foam. Note that secondary cracks are mainly parallel to the direction of fatigue load.

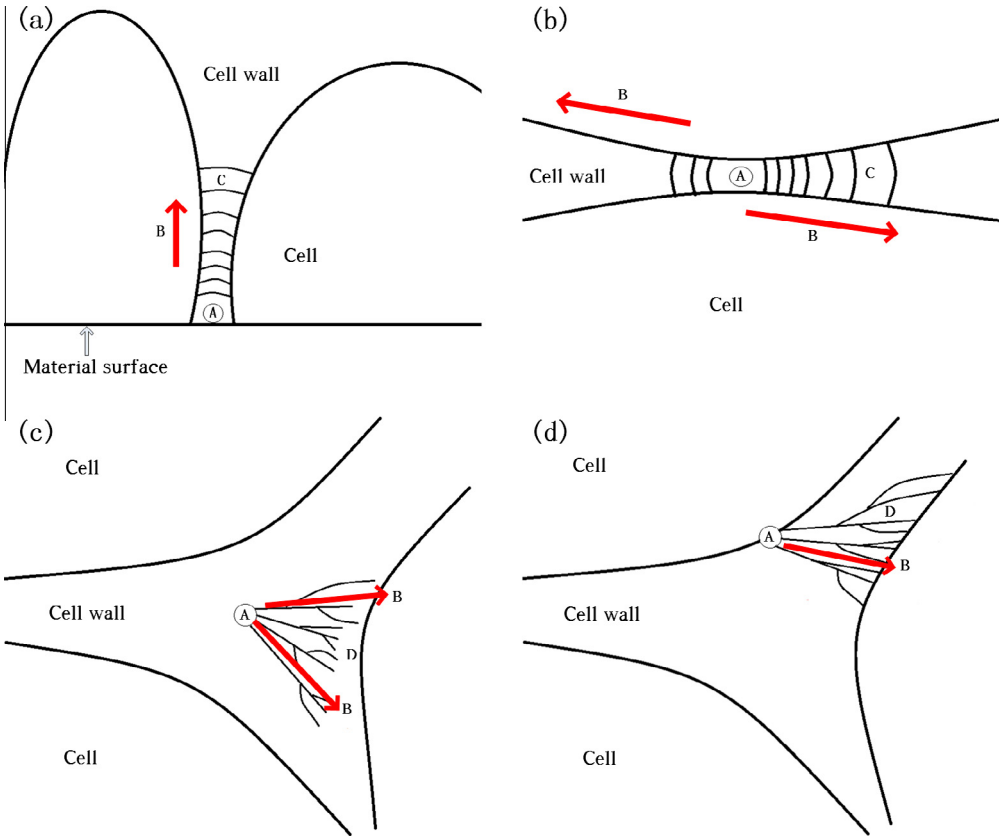

Fig. 13. Schematic diagrams for four categories of fracture mechanisms of the foam materials: (a) damage initiates from the material surface; (b) damage initiates on the cell walls; (c) damage initiates at the intersection of cell walls, and (d) damage initiates from the edge of one cell. The letters A, B, C and D represent the damage initiation position, damage propagation direction, fatigue striation and the river, and radial patterns, respectively.

the cell. Fatigue damage along cell walls and fatigue striations were also observed by Kolluri et al. [8] and Lin et al. [32] in fatigue tests of foams.

The third category of fatigue damage mechanism of the foam is damage initiation from the intersection region of cell walls, as shown in Fig. 10, where imperfection or stress concentration is commonly observed, and thus is prone to damage initiation. For Fig. 10, no obvious damage initiation position can be identified, which is quite different from the second category. However, typical river and radial patterns in the damage propagation regions (marked with red frames) still can be identified from Fig. 10. So, for this category the damage propagation region is firstly determined, which is indicated by the typical river and the radial pattern. Then, the damage initiation position can be inferred by reversing the damage propagation directions. The inferred damage initiation positions are marked with a black circle shown in Fig. 10. A small cell is found in the damage initiation position, which serves as a defect at the initial stage. Some defects are also observed along the damage propagation paths, which is reasonable since the damage propagation is in favor of the stress concentration sites. The final fracture regions are also shown in Fig. 10, in which typical dimple characteristics can be clearly seen.

The fourth category of fatigue damage mechanism is that damage initiates from the edge of one cell and propagates to the adjacent cell, as shown in Fig. 11. The stress concentration induced by existing micro-pores or defects at the edge of cell walls, which provide weak points for damage initiation and propagation, play a key role in the formation of damage. Similar to the third category of fatigue mechanism, it is hard to identify the damage initiation positions from adjacent zones by direct observation (Fig. 11). Damage initiation position can be determined by reversing the damage propagation directions.

Some secondary cracks appear on the fracture surface, which are parallel to the loading direction as indicated by white arrows in Fig. 12. Theoretically, the formations of secondary cracks may relate to both the misalignment of specimens and the irregular cell structure of foam material. In this work, the experiments are delicately designed to avoid the misalignment of specimens. As a consequence, the irregular microstructure of the foam induces secondary cracking.

The aforementioned fatigue mechanisms of the foam are summarized in Fig. 13, i.e. damage initiates from the surface of the specimen (Fig. 13(a)), on the cell walls (Fig. 13(b)), at the intersection of cell walls (Fig. 13(c)) and from the edge of cell (Fig. 13(d)), respectively.

5. Conclusions

The fatigue damage of closed-cell aluminum foam is experimentally investigated. Constant amplitude tension–tension fatigue tests are performed for the aluminum alloy foam, and the apparent elastic modulus within each loading cycle is obtained. It is found that the fatigue damage of the foam exhibits a large scatter, which is caused by the specimen-to-specimen variability. Then, a statistic fatigue damage model is developed in the framework of continuum damage mechanics, in which the statistical characteristic of fatigue damage of foam is described by using the normal distribution. The statistical damage model can describe the fatigue damage of foams.

To understand the damage mechanisms of the foam, scanning electron microscopy observation on the fracture surface of the foam specimen is carried out after the fatigue tests. It is observed that cracks initiate from different positions of foam material and the propagations of cracks are also different. Based on the experimental observation, four types of fatigue fracture mechanism in the foam are categorized, i.e. damage initiates from the material surface, damage initiates on the cell wall, damage initiates at the intersection of several cell walls and damage initiates from the edge of cell. Some secondary cracks which parallel to the loading direction are also found. The fatigue mechanisms are mainly governed by the irregular microstructure of the foam.

Acknowledgements

This work is supported by NSFC (11272246, 11321062 and 11272244).

References

[1] Gibson LJ, Ashby MF. Cellular solids-structure and properties. 2nd ed. Cambridge: Cambridge University Press; 1997.
[2] Xu ZM, Zhang WX, Wang TJ. Deformation of closed-cell foams incorporating the effect of inner gas pressure. Int J Appl Mech 2010;2:489–513.
[3] Qin QH, Wang TJ. An analytical solution for the large deflections of a slender sandwich beam with a metallic foam core under transverse loading by a flat punch. Compos Struct 2009;88:509–18.
[4] Qin QH, Wang MS, Wang ZJ, Zhang JX, Wang TJ. A yield criterion and plastic analysis for physically asymmetric sandwich beam with metal foam core. Int J Appl Mech 2013;5:1350037.
[5] Sugimura Y, Rabiei A, Evans AG, Harte AM, Fleck NA. Compression fatigue of a cellular Al alloy. Mater Sci Eng, A 1999;269:38–48.
[6] Zettl B, Mayer H, Tschegg SES, Degischer HP. Fatigue properties of aluminum foams at high numbers of cycles. Mater Sci Eng, A 2000;292:1–7.
[7] McCullough KYG, Fleck NA, Ashby MF. The stress-life fatigue behaviour of aluminium alloy foams. Fatigue Fract Eng Mater Struct 2000;23:199–208.
[8] Kolluri M, Mukherjee M, Garcia-Moreno F, Banhart J, Ramamurty U. Fatigue of a laterally constrained closed cell aluminum foam. Acta Mater 2008;56:1114–25.
[9] Zenkert D, Burman M. Tension, compression and shear fatigue of a closed cell polymer foam. Compos Sci Technol 2009;69:785–92.
[10] Kanny K, Mahfuz H, Carlsson LA, Thomas T, Jeelani S. Dynamic mechanical analyses and flexural fatigue of PVC foams. Compos Struct 2002;58:175–83.
[11] Olurin OB, McCullough KYG, Fleck NA, Ashby MF. Fatigue crack propagation in aluminium alloy foams. Int J Fatigue 2001;23:375–82.
[12] Motz C, Friedl O, Pippan R. Fatigue crack propagation in cellular metals. Int J Fatigue 2005;27:1571–81.
[13] Zenkert D, Shipsha A, Burman M. Fatigue of closed cell foams. J Sand Struct Mater 2006;8:517–38.
[14] Zhou J, Soboyejo WO. Compression–compression fatigue of open cell aluminum foams: macro-/micro-mechanisms and the effects of heat treatment. Mater Sci Eng, A 2004;369:23–35.
[15] Ingraham MD, DeMaria CJ, Issen KA, Morrison DJ. Low cycle fatigue of aluminum foam. Mater Sci Eng, A 2009;504:150–6.
[16] Lemaitre J, Plumtree A. Application of damage concepts to predict creep–fatigue failures. J Eng Mater – Trans ASME 1979;101:284–92.
[17] Wang TJ, Lou ZW. A continuum damage model for weld heat affected zone under low cycle fatigue loading. Eng Fract Mech 1990;37:825–9.
[18] Lemaitre J. Coupled elasto-plasticity and damage constitutive equations. Comput Methods Appl Mech Eng 1985;51:31–49.
[19] Wang TJ. A continuum damage model for ductile fracture of weld heat affected zone. Eng Fract Mech 1991;40:1075–82.
[20] Wang TJ. Unified CDM model and local criterion for ductile fracture-I. Unified CDM model for ductile fracture. Eng Fract Mech 1992;42:177–83.
[21] Ramamurty U, Paul A. Variability in mechanical properties of a metal foam. Acta Mater 2004;52:869–76.
[22] Zhu HX, Windle AH. Effects of cell irregularity on the high strain compression of open-cell foams. Acta Mater 2002;50:1041–52.
[23] Simon AE, Gibson LJ. Aluminum foams produced by liquid state process. Acta Mater 1998;46:3109–23.
[24] Brothers AH, Dunand DC. Plasticity and damage in cellular amorphous metals. Acta Mater 2005;53:4427–40.
[25] Andrews EW, Huang JS, Gibson LJ. Creep behavior of a closed-cell aluminum foam. Acta Mater 1999;47:2927–35.
[26] Zhao MD, Fan XL, Fang QZ, Wang TJ. Experimental investigation of the fatigue of closed-cell aluminum alloy foam. Mater Lett 2015;160:68–71.
[27] Huang S, Zhou JZ, Sheng J, Lu JZ, Sun GF, Meng XK, et al. Effects of laser energy on fatigue crack growth properties of 6061-T6 aluminum alloy subjected to multiple laser peening. Eng Fract Mech 2013;99:87–100.
[28] Lemaitre J, Dufailly J. Damage measurements. Eng Fract Mech 1987;28:643–61.
[29] Lemaitre J. A continuous damage mechanics model for ductile fracture. J Eng Mater Technol 1985;107:83–9.
[30] Lemaitre J. How to use damage mechanics. Nucl Eng Design 1984;8:233–46.
[31] Dhar S, Dixit PM, Sethuraman R. A continuum damage mechanics model for ductile fracture. Int J Pres Ves Pip 2000;77:335–44.
[32] Lin JG, Zhang YF, Ma M. Preparation of porous Ti35Nb alloy and its mechanical properties under monotonic and cyclic loading. Trans Nonferrous Met Soc China 2010;20:390–4.